CrossMark

Crystal structure and biochemical characterization of Chlamydomonas FDX2 reveal two residues that, when mutated, partially confer FDX2 the redox potential and catalytic properties of FDX1

Marko Boehm[1] · Markus Alahuhta[1] · David W. Mulder[1] · Erin A. Peden[1] ·
Hai Long[2] · Roman Brunecky[1] · Vladimir V. Lunin[1] · Paul W. King[1] ·
Maria L. Ghirardi[1] · Alexandra Dubini[1]

Abstract The green alga *Chlamydomonas reinhardtii* contains six plastidic [2Fe2S]-cluster ferredoxins (FDXs), with FDX1 as the predominant isoform under photoautotrophic growth. FDX2 is highly similar to FDX1 and has been shown to interact with specific enzymes (such as nitrite reductase), as well as to share interactors with FDX1, such as the hydrogenases (HYDA), ferredoxin:NAD(P) reductase I (FNR1), and pyruvate:ferredoxin oxidoreductase (PFR1), albeit performing at low catalytic rates. Here we report the FDX2 crystal structure solved at 1.18 Å resolution. Based on differences between the *Chlorella fusca* FDX1 and *C. reinhardtii* FDX2 structures, we generated and purified point-mutated versions of the FDX2 protein and assayed them in vitro for their ability to catalyze hydrogen and NADPH photo-production. The data show that structural differences at two amino acid positions contribute to functional differences between FDX1 and FDX2, suggesting that FDX2 might have evolved from FDX1 toward a different physiological role in the cell. Moreover, we demonstrate that the mutations affect both the midpoint potentials of the FDX and kinetics of the FNR reaction, possibly due to altered binding between FDX and FNR. An effect on H_2 photo-production rates was also observed, although the kinetics of the reaction were not further characterized.

Abbreviations

CD	Circular dichroism
DCMU	(3-(3,4-Dichlorophenyl)-1,1-dimethylurea)
DCPIP	2,6-Dichlorophenolindophenol
DMSO	Dimethyl sulfoxide
DTT or NaDT	Sodium dithionite
EPR	Electron paramagnetic resonance
FAD	Flavin adenine nucleotide
FDX	Ferredoxin
FNR	Ferredoxin/NADP(H) oxidoreductase
FPLC	Fast protein liquid chromatography
GST	Glutathione S-transferase
HYDA	Algal hydrogenase
NADP(H)	Nicotinamide adenine dinucleotide phosphate-oxidase
PCR	Polymerase chain reaction
PFR1	Pyruvate/ferredoxin oxidoreductasePDB, protein database
RT	Room temperature
TEV	Tobacco etch virus protease

Marko Boehm and Markus Alahuhta authors have contributed equally to the work.

Electronic supplementary material The online version of this article (doi:10.1007/s11120-015-0198-6) contains supplementary material, which is available to authorized users.

✉ Alexandra Dubini
alexdubini@yahoo.com; alexandra.dubini@nrel.gov

[1] Biosciences Center, National Renewable Energy Laboratory, Mail Stop: 3313, 15013 Denver West Parkway, Golden, CO 80401, USA

[2] Computational Science Center, National Renewable Energy Laboratory, 15013 Denver West Parkway, Golden, CO 80401, USA

Introduction

Ferredoxins (FDXs) are small, ubiquitous proteins that typically contain iron-sulfur clusters and mediate electron shuttling among multiple metabolic pathways. The green

alga *Chlamydomonas reinhardtii* (Chlamydomonas throughout) contains six genes that encode for chloroplast-localized ferredoxins. These proteins have been categorized into three separate groups, according to the plant nomenclature: FDX1 and FDX5 belong to the photosynthetic category (or leaf type), FDX2 belong to the non-photosynthetic group (or root type), and FDX3, FDX4, and FDX6 are divergent, being more closely related to bacterial FDXs (Terauchi et al. 2009). In their oxidized state, FDXs display absorption maxima in the visible region at about 330, 420, and 464 nm, and their redox potentials are very negative; FDX1, for example, is centered at around −398 mV (Wada et al. 1974; Orme-Johnson 1973; Matsubara and Sasaki 1968; Hutson et al. 1978; Hase et al. 1976). FDXs harbor a $CX_4CX_2CX_nC$ motif required for [2Fe2S]-cluster ligation and form specific electrostatic complexes with a variety of interacting enzymes, using carboxyl side-chain groups of conserved amino acids that generally interact with lysine or arginine counterparts on the binding partner.

As electron shuttles, Chlamydomonas FDXs are particularly important for hydrogen production, because they are the natural electron donor to the hydrogenases in vivo. Chlamydomonas contains two [FeFe]-hydrogenase enzymes, *Cr*HYDA1 and *Cr*HYDA2, which catalyze the formation of hydrogen from two electrons and two protons, either under light-anoxic or dark-anoxic conditions (Ghirardi et al. 2000; Harris 2009). FDXs represent a branch point for three hydrogen production pathways (Meuser et al. 2012; Winkler et al. 2010): the PSII dependent, PSII independent, and fermentative.

To further characterize the role of the algal FDXs, Peden et al. (2013) identified specific targets for each of the six Chlamydomonas FDXs and assessed *Cr*FDX1 and *Cr*FDX2 specificity toward selected metabolic pathways. Using yeast two-hybrid and pull-down assays, they detected binding partners for the two *Cr*FDXs and confirmed that *Cr*FDX2 can also interact with common *Cr*FDX1 interaction partners. *Cr*FDX2 amino acid sequence is highly homologous to that of *Cr*FDX1 (67 % identity for the mature proteins), and it contains conserved residues that are known to be important for interactions with *Cr*FDX1 enzyme targets (Winkler et al. 2009b). This sequence conservation might explain why *Cr*FDX2 participates in electron-transfer reactions with similar redox partners as *Cr*FDX1, although at lower rates. Both proteins contain three highly conserved, negatively charged, solvent-exposed regions that were proposed to be responsible for mediating protein–protein interactions in FDXs (Kameda et al. 2011). Typically, these regions form a highly conserved structure that facilitates cluster insertion to the apo-protein and electron transfer to/from the mature protein (Bertini et al. 2002; Kameda et al. 2011). Four conserved amino acid residues present in the two *Cr*FDXs

specifically contribute to electron donor/acceptor selectivity in vivo (Terauchi et al. 2009). Indeed, *Cr*FDX2 has recently been shown to mediate electron transfer (although not as efficiently as *Cr*FDX1) to known *Cr*FDX1 interaction partners, i.e., *Cr*FNR1, *Cr*HYDA1, and *Cr*PFR1, (Noth et al. 2012; Peden et al. 2013; Terauchi et al. 2009; van Lis et al. 2013). However, it is unknown whether or under which conditions this happens in vivo.

Structural models have predicted differences in surface charge distribution on the two *Cr*FDXs, which may explain *Cr*FDX1′s more negative redox potential (−398 vs −321 mV for *Cr*FDX2) (Galván and Márquez 1985; Terauchi et al. 2009). These distinct physical characteristics might determine their interaction specificity and influence the binding of various electron acceptors/donors to each protein (Terauchi et al. 2009). Notably, *Cr*FDX2 lacks a phenylalanine (F62) residue that may be required for the proper interaction of *Cr*FDX1 with *Cr*HYDA (Winkler et al. 2009a) and possibly with *Cr*FNR1 (Hurley et al. 1997; Mayoral et al. 2005); it also lacks a C-terminus tyrosine residue, Y95, present in *Cr*FDX1. The lower capability of *Cr*HYDA1 to generate hydrogen using *Cr*FDX2 as the electron donor might be indicative not only of their different redox potentials but also of different interaction mechanisms between *Cr*HYDA1 and either *Cr*FDX1 or *Cr*FDX2.

In an effort to better define these interactions and the function of *Cr*FDX1 and *Cr*FDX2, we over-expressed the two proteins in *E. coli*. The mature versions of these proteins were purified, used for crystallography studies, and characterized by different types of spectroscopic techniques (see supplemental data 1, 2, 3, and 4). Here we report the first 3D structure of a Chlamydomonas ferredoxin, *Cr*FDX2, at atomic resolution of 1.18 Å. The *Cr*FDX2 folding motif is similar to that of previously published plant-type FDX structures from other organism (Bes et al. 1999; Fish et al. 2005), one of which represents a FDX1 type from *Chlorella fusca* (*Cf*), with high sequence homology to the noncrystallized *Cr*FDX1. Based on the high degree of similarity between *Cf* and *Cr* FDX1, comparison with the *Cr* FDX2 structure, and published data, we selected two amino acid residues present on the interaction surface of *Cr*FDX1 with FNR and hydrogenase (but absent or present as a different residue on *Cr*FDX2). We mutated *Cr*FDX2 F62 to M62 (the equivalent residue in *Cr*FDX1) and inserted Y95 into *Cr*FDX2 through site-directed mutagenesis. We show that mutations that replace these residues with those found in *Cr*FDX1 lower *Cr*FDX2′s midpoint redox potential to values closer to that of *Cr*FDX1, indicating that these residues contribute to functional differences between *Cr*FDX1 and *Cr*FDX2. The major observed difference consisted of altered midpoint redox potential of the FDX cluster, resulting in changes in its catalytic efficiency with respect to FNR-mediated $NADP^+$ reduction, as well as alterations in the

maximum rates of hydrogenase-catalyzed H_2 photo-production in vitro.

Materials and methods

Plasmid construction

We constructed several over-expression plasmids for all the mature, codon-optimized (Mr. Gene, Germany) versions of the Chlamydomonas FDX proteins, using a modified version of the pRSETA vector (Life Technologies, USA; Michoux et al. 2010) as the backbone. For the pull-down experiments, we used N-terminal His-tagged *Cr*FDX1 and *Cr*FDX2 proteins that were expressed from the pRESTA His-FDX1 and pRESTA His-FDX 2 expression constructs, respectively. For this, the *Cr*FDX1 and *Cr*FDX2 coding sequences were amplified using FDX1 primers (Peden et al. 2013) and the following FDX2 primers: FDX2-Fw GGATCCTTCAAAGTCACCTTCAAAA CCCCAAAAGGTG-3′ and FDX2-Rev 5′-ACATCGTCA TTTTAACCGATCAAGAATCAAAATTGTGAGAAT TC-3. The amplified gene sequences were cloned into the BamHI and EcoRI restriction sites on the vector. The tobacco etch virus protease (TEV)-cleaved versions of the *Cr*FDX1 and *Cr*FDX2 proteins were expressed as His-GST-TEVcs-FDX1 and His-GST-TEVcs-FDX2 fusion proteins and contained a linker sequence (Yacoby et al. 2012) between the His-GST tandem affinity tag and the FDX sequence. These versions were used for UV/Vis and EPR spectroscopy. The cleaved versions of the *Cr*FDX1 and *Cr*FDX2 proteins used for CD spectroscopy that yielded *Cr*FDX2 crystals for X-ray crystallography were expressed as FDX1-TEVcs-GST-His and FDX2-TEVcs-GST-His fusion proteins that contained the same linker sequence (Yacoby et al. 2012) between the FDX and the GST-His tandem affinity tag. To generate the expression constructs for the point-mutated *Cr*FDX2 s (M62F, ∇95Y and M62F/∇95Y), the C-terminal-encoding fragment of the *Cr*FDX2 protein was excised from the His-GST-TEVcs-FDX2 construct using HincII and EcoRI. Subsequently, digested PCR fragments generated with the following primers replaced the excised fragment: (A) *Cr*FDX2 M62F: Fw 5′-GCGGTCGA CCAATCCGACCAAAACTTTTTGGACGAAGATCAA TTG-3′, (B) *Cr*FDX2 M62F Rv: 5′-GGAATTCTCACAAT TTTGATTCTTGATC.

GGTTAAAATGACGATGT-3′, (C) *Cr*FDX2 ∇Y95 Fw: 5′-GCGTACTGTCGACCAATCCGACCAA.

AACATG-3′, and (D) *Cr*FDX2 ∇Y95 Rev: 5′-GAAT TCTCAGTACAATTTTGATTCTTGATCGGTTAAAAT GACGATGT-3′. The appropriate primer combinations were used to introduce the two point mutations into the WT FDX2.

Protein purification

The *Cr*FDX1 and *Cr*FDX2 over-expression plasmids were transformed into *E. coli* KRX cells (Promega, USA). For expression in Terrific Broth with 200 µg/ml Ampicillin (TB; VWR, USA), a starter culture was grown overnight at 37 °C and diluted 1:100 in a 100-ml TB subculture the following morning. After the subculture had reached an OD600 of ∼0.7, 10 ml of it were used to inoculate 1 L of TB media supplemented with 0.4 % (w/v) glycerol. At OD600 of ∼0.7, IPTG and Ferric ammonium citrate were added to final concentrations of 1 mM and 0.05 % (w/v), respectively, (Peden et al. 2013). The cells were harvested and resuspended in 100 ml lysis buffer (25 mM Tris pH 7.9, 100 mM NaCl, and 1 mM DTT) for breakage. The supernatant obtained after centrifugation was incubated for 1 h at 4 °C with 20 ml of glutathione affinity resin (Genscript, USA). After the incubation period, the resin was washed with 15 column volumes (CV) of lysis buffer or until the wash solution became clear and colorless. Protein elution was performed with $2 \times CV$ of elution buffer (25 mM Tris pH = 7.9, 100 mM NaCl, and 10 mM reduced glutathione). 20 mg of TEV-His (His-tag purified from pRK193 (Kapust et al. 2001; Addgene, USA) were added to cleave the affinity tag. After a 2-h incubation period at RT, the sample was applied to a TALON Cobalt affinity chromatography column (∼20 ml resin (Clontech, USA) packed in a XK16/20 (GE Healthcare column) coupled to an Äkta FPLC (GE Healthcare, USA), see supplemental Fig. 1. We used 25 mM Tris pH 7.0, 100 mM NaCl, and 5 % (v/v) glycerol as the running buffer at a flow rate of 5–10 ml min^{-1}. The flow-through was collected and loaded onto a HiLoad^{TM} 26/60 Superdex^{TM} 75 prep grade (GE Healthcare, USA) following the purification method developed by Peden et al. (2013). The iron content was determined using a colorimetric assay described (Winkler et al. 2009b), which uses ferrozine under reductive conditions after digestion of the protein in 4.5 % (w/v) KMnO4 and 1.2 N HCl.

Protein crystallization

*Cr*FDX2 protein crystals were obtained by the sitting drop vapor diffusion method, using a 96-well plate with Crystal Screen HT (Hampton Research, USA). Fifty µL of well solution were added to the reservoirs and drops were made with 0.2 µL of well and 0.2 µL of protein solution using a Phoenix crystallization robot (Art Robbins Instruments, USA). Protein crystals grew at 20 °C in 0.1 M HEPES pH 7.0 and 3.2 M ammonium sulfate as the well solution. The protein solution contained 17.3 mg/ml of protein in 25 mM Tris pH 7.0, 200 mM NaCl, and 5 % (v/v) glycerol.
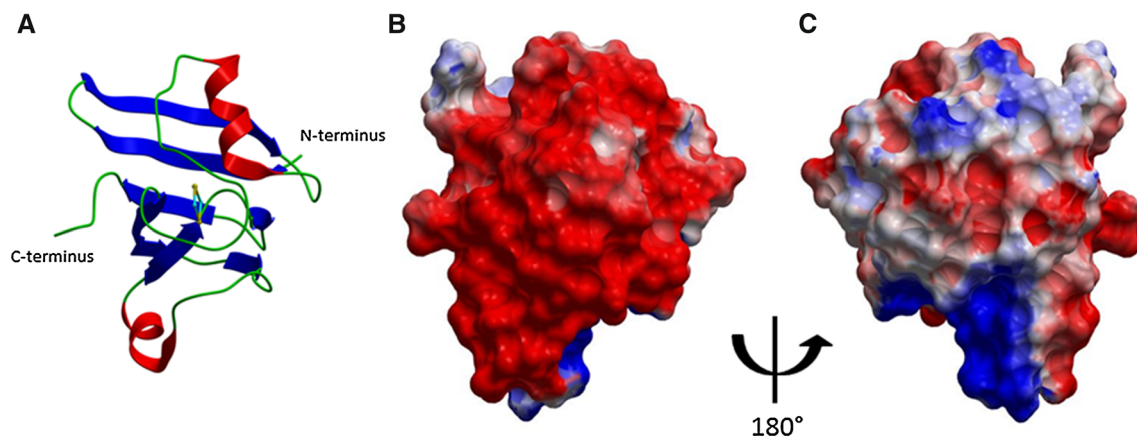
Fig. 1 *Cr*FDX2 secondary structure and surface charge distribution models. **a** Ribbon diagram of the *Cr*FDX2 structure with the [2Fe2S] cluster. N- and C-termini are indicated. Loops are shown as *green* ribbons; α-helices are in *red* and β-strands in *blue*; the [2Fe2S] cluster is shown in ball and stick format, with sulfur in yellow and iron atoms in cyan. **b**, **c** Electrostatic surfaces charges are shown in *red* (negative) and *blue* (positive). *Panel B* is shown in the same orientation as *Panel A* and represents a straight-on view of the [2Fe2S] cluster. *Panel C* is rotated 180° with respect to *panels A* and *B*. The orientation chosen here highlights the different-charged region of *Cr*FDX2 with the *red region* being the area of *Cr*FNR/*Cr*HYDA1 interaction

Data collection and processing

The *Cr*FDX2 protein crystal was flash-frozen in a nitrogen gas stream at 100 K before data collection, using an in-house Bruker × 8 MicroStar X-Ray generator with Helios mirrors and Bruker Platinum 135 CCD detector. A well solution containing 5 % (v/v) glycerol and 5 % (v/v) ethylene glycol was added into the drop before freezing to prevent ice formation. Data were indexed and processed with the Bruker suite of programs version 2011.2-0 (Bruker AXS, USA).

Structure solution and refinement

Intensities obtained from data processing (derived from diffraction intensities) were converted into structure factors and 5 % of the reflections were flagged for Rfree calculations using the programs SCALEPACK2MTZ, ctruncate, MTZDUMP, Unique, CAD, FREERFLAG, and MTZU-TILS from the CCP4 package (Winn et al. 2011). The program MrBUMP version 0.6.1 (Winn et al. 2011) automatically solved the structure using the FASTA (Pearson and Lipman 1988) and MOLREP (Vagin and Teplyakov 2010) programs for sequence searches and molecular replacement. Refinement and manual correction were performed using the REFMAC5 (Murshudov et al. 2011) version 5.7.0032 and the Coot (Emsley et al. 2010) version 0.6.2 programs. The MOLPROBITY method (Chen et al. 2010a) was used to analyze the Ramachandran plot, and root mean square deviations (rmsd) of bond lengths and angles were calculated from ideal values of Engh and Huber stereochemical parameters (Engh and Huber 1991). The Wilson B-factor was calculated using the ctruncate version 1.5.1, and average B-factors were calculated using

the ICM version 3.7-2a program (Molsoft LLC, USA). Coot, PyMOL (http://www.pymol.org), and ICM (http://www.molsoft.com) were used for comparing and analyzing structures. Figure 1 was done using ICM and PyMOL was used to make Fig. 2. The data collection and refinement statistics are shown in Table 1.

Isolation of thylakoids

In order to generate the thylakoids membrane for the H_2 and NADP assays, Chlamydomonas cells were harvested from cultures grown in Tris/Acetate/Phosphate medium (TAP) (pH 7.2) (Harris 2009). Algal cultures were maintained at 25 °C, vigorously bubbled with air enriched with 3 % (v/v) CO_2, stirred using a magnetic stirrer bar, and illuminated with continuous light of 80 µmol photon m^{-2} s^{-1}. These cells were then washed with 1/5 volume of buffer 1 (containing 1 0.35 M sorbitol, 20 mM HEPES, pH 7.5, 2.0 mM MgCl2) and repellet as above. The cells were broken using a french press and the thylakoids were pelleted at 40,000 × G (for 20 min at 4 °C). The final thylakoids were resuspended in equal or greater volume of buffer 1, homogenized and spinned at 1200 × G for 30 s to pellet unbroken cells. The supernatant was removed and the pelleted thylakoids stored at −80 °C at with a final concentration of 1.0 mg Chl^{-1} ml^{-1}.

Hydrogen photo-production

A master mix was prepared for the hydrogen photo-production assay as follows (amount per assay): 900 ml buffer A (50 mM tris–HCl pH 7.4, 3.35 mg ml^{-1} bovine serum albumin, 10 mM MgCl₂, and 200 mg ml^{-1} sucrose), 5 µL of DCPIP (0.01 mM in buffer A), 10 µL of DCMU
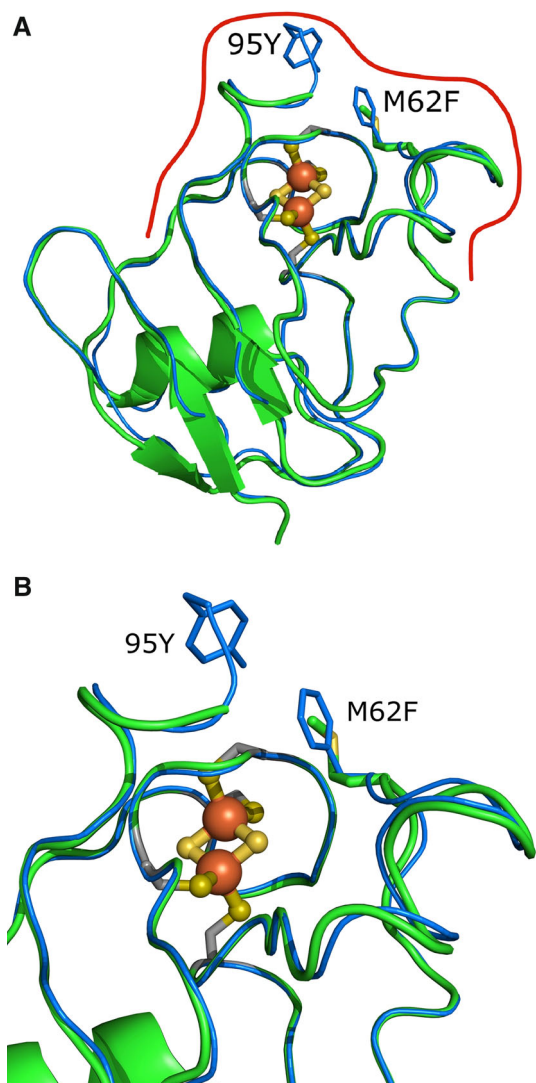
Fig. 2 *Cr*FDX2 binding interface with *Cr*HYDA1/*Cr*FNR1 and point mutations. **a** Overall view of *Cr*FDX2 superimposed with *Cf*FDX1. Mutations and the approximate binding interface area indicated by a *red line*. **b** Closer view of the mutations. *Coloring* The backbone of *Cr*FDX2 is shown as *green ribbon* and *Cf*FDX1 backbone is shown in *blue*; oxygen atoms are *red*, nitrogen atoms are *blue*, sulfur atoms are *yellow*, and the coordinating cysteine side-chain carbons are *colored gray*. The [2Fe2S] cluster is shown in ball and stick, with sulfur in *yellow* and iron in *orange*. The main chains of the residue stick representations have been hidden for clarity

Table 1 X-ray data collection and refinement statistics for *Cr*FDX2 crystal structure

Data collection	
Space group	P1
Unit cell (Å, °)	$a = 25.429$, $b = 26.458$, $c = 31.016$
	$\alpha = 102.56$, $\beta = 104.35$, $\gamma = 100.30$
Wavelength (Å)	1.54178
Temperature (K)	100
Resolution (Å)	25–1.18 (1.28–1.18)
Unique reflections	24232 (5195)
R_{int}^a	0.0838 (0.2948)
Average redundancy	6.1 (2.3)
$<I>/<\sigma(I)>$	11.9 (2.6)
Completeness (%)	99.4 (98.1)
Resolution (Å)	25–1.18 (1.21–1.18)
R/R_{free}	0.109 (0.246)/0.147 (0.305)
Protein atoms	
Water molecules	
Other atoms	
RMSD from ideal bond length (Å)[b]	0.024
RMSD from ideal bond angles (°)[b]	2.497
Wilson B-factor	
Average B-factor for protein atoms (Å²)	
Average B-factor for water molecules (Å²)	
Ramachandran plot statistics (%)[c]	
Allowed	100
Favored	98.7
Outliers	0

Statistics for the highest resolution bin are in parenthesis

[a] $Rint = \sum|I - <I>|/\sum|I|$ where I is the intensity of an individual reflection and $<I>$ is the mean intensity of a group of equivalents, and the sums are calculated over all reflections with more than one equivalent measured

[b] Chen et al. (2010b)

[c] Chen et al. (2010a)

(0.3 mM in DMSO), 10 µL of sodium ascorbate (1 M), 10 µL glucose oxidase (30 mg/ml in buffer A), 50 µL glucose (1 M), 10 µL catalase (10 mg ml^{-1} in buffer A), 50 µL 96 % (v/v) ethanol, and 100 nM HYDA1 hydrogenase (in buffer A), as described previously (24). All solutions had been previously degassed and were mixed inside a MBRAUN glove box in a 100 % N_2 atmosphere. FDX was placed in 9-ml serum vials containing the master mix to a final concentration of 10 mM. After addition of

Chlamydomonas thylakoids to a final concentration of 25 mg ml^{-1} chlorophyll in the dark, 1.2 ml of the master mix were transferred to serum vials. The vials were sealed with rubber septa and wrapped in aluminum foil. A zero time-point sample was taken, the vial was unwrapped, and illuminated at 400 µmol photons m^{-2} s^{-1} generated by a LED light source (2000 W Diamond Series, www.advancedLEDlights.com). Hydrogen in the head-space was measured at different time points by a gas chromatograph (400 µl injection volume), and the resulting hydrogen production rates were calculated using data from three

replicate samples for each FDX tested (μmol H_2 μg Chl^{-1} h^{-1}).

NADPH photo-production

Initially, three solutions were prepared: (a) a buffer master mix containing (for each FDX/concentration combination) 1 μl of DCMU (0.3 mM in DMSO), 2.5 μl of DCPIP (0.01 mM), 5 μl of sodium ascorbate (1 M), Chlamydomonas thylakoids to a Chl concentration of 50 μg ml^{-1} (in the final assay) and buffer A (see above) to a total volume of 268 μl per buffer master mix; (b) a protein mix (final volume of 208 μl) containing 0.5 μM Chlamydomonas FNR1 (expressed in and purified from *E. coli*) and various concentrations of FDXs (FDX1, FDX2, FDX2 M62F, FDX2 ∇95Y, and FDX2 M62F/∇95Y), and (c) a 0.04 mM $NADP^+$ solution. For each assay, 8 μl of the $NADP^+$ solution were placed in a well of a 96-well plate. Then, in the dark, 208 μl of the buffer master mix were added to each protein mix and 130 μl of this mixture were added to three separate wells (triplicate samples). The plate was kept in the dark ($t = 0$ was taken) and then illuminated at 300 μmol photons m^{-2} s^{-1} from an LED light source (2000 W Diamond Series, www.advancedLEDlights.com). Further absorbance measurements were taken at various time points and recorded by the Infinite M200Pro plate reader (Tecan, USA). NADPH production rates (μmol NADPH μg Chl^{-1} h^{-1}; for FNR1 at 1 mM in a final volume of 1 ml) were calculated based on a NADPH standard curve to determine the amount of NADPH produced in the assay (assay volume is 138 μl). Subsequently, the inverse of the rates were plotted over the inverse of the FDX concentrations in a Lineweaver–Burk plot and both K_m and V_{max} values were calculated for three replicates of each FDX and concentration combinations.

EPR monitored redox titrations

Potentiometric titrations of FDX2 mutants and FDX2 for reference were carried out anaerobically in a MBraun box (N_2 atmosphere, 25 °C) using an ORP triode electrode (internal Ag/AgCl reference, platinum sensor, Thermo Scientific 9678BNWP). The electrode was connected via a BNC cable to a pH meter (Oakton) operating in relative mV mode and calibrated to a standard solution (Orion 967901). All values were adjusted +200 mV and reported versus the normal hydrogen electrode (NHE) potential. The reaction was carried out in a custom vessel (Allen Scientific Glass, Boulder CO) with magnetic stirring using a similar reductive titration procedure as described previously (Usselman et al. 2008). NaDT was used as the

reductant and added in 2 uL increments (2 mM stock) with a Hamilton repeating dispenser to the protein (2–5 mg/mL) buffer solution (50 mM Tris pH 7.8, 100 mM NaCl, 20 % glycerol). The protein buffer solution was supplemented with a redox mediator cocktail (3 μM final concentration) to allow for fast equilibrium between protein and reductant (Dutton 1978). The cocktail consisted of indigo disulfonate ($E_m = -255$ mV vs NHE), phenosafranine ($E_m = -255$ mV vs NHE), benzyl viologen ($E_m = -361$ mV vs NHE), and methyl viologen ($E_m = -440$ mV vs NHE). Samples at poised redox potentials were removed from the vessel after several minutes of equilibration following NaDT addition at roughly 20 mV increments and transferred to 4 mM EPR tubes (Wilmad LabGlass). EPR tubes were sealed with septa and frozen in liquid nitrogen.

EPR spectra were recorded on a Bruker ELEXSYS E500 CW X-band spectrometer system outfitted with an Oxford Instruments cryostat and temperature controller and cylindrical (SHQ) Bruker resonator. Spectra were collected at optimal power and temperature settings (1.0 mW, 23 ± 3 K) as determined from power saturation and temperature analysis of reduced wild-type samples (Supplemental Fig. 3). Other spectrometer settings were as follows: microwave frequency, 9.385 GHz; modulation frequency, 100 kHz; modulation amplitude, 10.0 G; and time constant, 327.68 ms. Simulations of the spectra were carried out in EasySpin (Stoll and Schweiger 2006).

To determine the midpoint potential (E_m) of the $[2Fe2S]^{2+/1+}$ cluster, plots of signal amplitude of the reduced $[2Fe2S]^{1+}$ signal (measured at the $g = 2.05/2.06$ peak) versus sample potential (E) were fitted a form of the $n = 1$ Nernst equation (Hagen 2008).

$$[\text{Red}] = \frac{[\text{Ox}] + [\text{Red}]}{1 + \exp((E - E_m)/0.026)}$$

Fits were carried out using the nonlinear least-squares curve fitter in OriginPro. Errors in the E_m values are estimated at ± 6 mV from the standard error of the fits and voltage readouts during the experiment.

Results

Crystal structure of CrFDX2

The structure of *Cr*FDX2 was refined to a resolution of 1.18 Å with R and Rfree of 0.109 and 0.147, respectively (Fig. 1). There is only one molecule in the asymmetric unit in complex with the [2Fe2S] cluster (Fig. 1a), and it shows a typical ferredoxin fold with a β-sheet formed by five β-strands covered by a single α-helix (Fukuyama 2004). The [2Fe2S] cluster of *Cr*FDX2 is coordinated by four cysteine
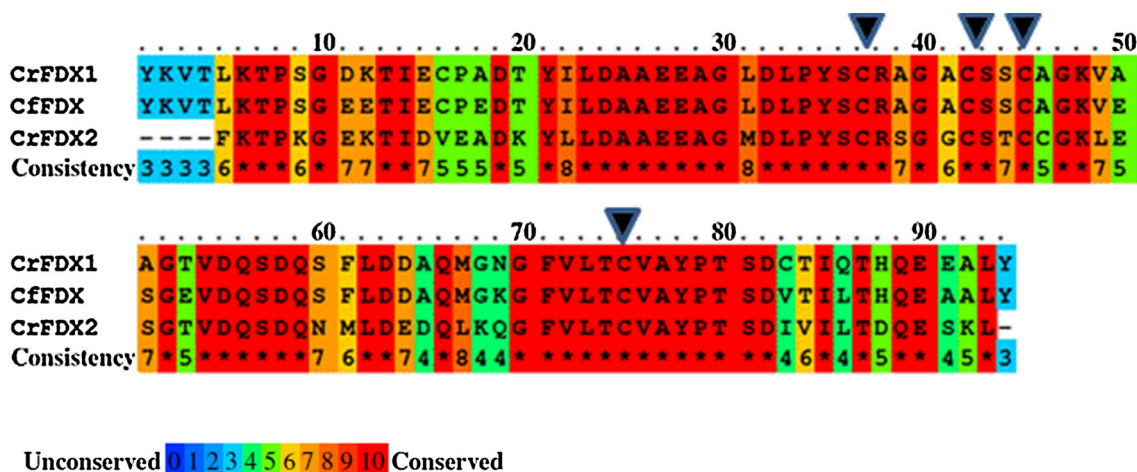
Fig. 3 Protein sequence alignment for *Cr*FDX1, *Cr*FDX2, and *Cf* FDX. The protein sequences of the mature *Cr*FDX1, *Cr*FDX2 and *Cf*FDX proteins were aligned using the Praline multiple sequence alignment tool (http://www.ibi.vu.nl/programs/pralinewww/), and they highlight amino acid conservation among the three proteins (the three sequences show 75 % similarities). The *arrowheads* indicate the [2Fe2S]-cluster coordinating cysteine residues C37, C42, C45, and C75. All numbering differs by 1 due to the lack of the M at the start, which is present in the recombinant protein of the *Cr*FDXs

residues: Cys38, Cys 43, Cys 46, and Cys 76 (Fig. 2a, b; the numbering differs from that in Fig. 3 by 1, due to the lack of M at the start of each recombinant protein sequence). This structure has been deposited into the protein data bank (PDB; www.rcsb.org) with entry code 4ITK.

Structural comparison with other FDXs

Pair-wise secondary structure matching by the PDB-fold program (Krissinel and Henrick 2004) found 60 unique structural matches for *Cr*FDX2 from the protein data bank with at least 70 % secondary structure similarity. Out of these, the first 53 were [2Fe2S]-ferredoxins and the remaining 7, although having high protein fold similarity to *Cr*FDX2, showed less than 20 % sequence similarity with it. The most similar match to *Cr*FDX2 was the cyanobacterium *Mastigocladus laminosus* [2Fe2S]-FDX (PDB ID: 1RFK; (Fish et al. 2005)), with a secondary structure similarity of 100 %, sequence similarity of 66 %, and Cα root mean square deviation of 0.84 Å^2, suggesting similar backbones between the two proteins. Further inspections of similar ferredoxin structures showed significant variability between the positions of the backbone atoms away from the iron-sulfur cluster. This was the case even when the overall structure seemed to be highly similar. To properly find similar structures that might have been missed by the structural similarity search, we searched the PDB using sequence homology with the ICM program and found 36 structures with sequence similarity above 25 %. The best hit was *Chlorella fusca* FDX1 (*Cf*FDX1, PDB ID: 1AWD Bes et al. 1999) with sequence similarity of 68 % and Cα root mean square deviation of 0.79 Å^2. Closer inspection of this structure showed that it indeed was highly similar to *Cr*FDX2.

Algal *Cr*FDX1/*Cr*FDX2 binding interface with *Cr*HYDA1/*Cr*FNR1 and point mutations

The *Cr*FDX1 and *Cr*FDX2 proteins are highly homologous, with 67 % sequence identity (Fig. 3). Furthermore, *Cr*FDX2 (a root-type ferredoxin Terauchi et al. 2009) shares a practically identical protein backbone with the leaf-type *Cf*FDX1 (Fig. 3) indicating that both FDX types would be expected to share the same binding interface with *Cr*HYDA1/*Cr*FNR1 (Fig. 2a). For this interaction, we assumed that the binding interface is centered on the iron-sulfur cluster, based on a thorough analysis of related binding interfaces from literature (Chang et al. 2007; Hurley et al. 1993a, b; Morales et al. 2000). The distance between the iron-sulfur clusters is crucial for electron tunneling. According to known structures and computer modeling of electron tunneling enzyme complexes, the edge-to-edge distances should not exceed 14 Å in the absence of other additional cofactors to act as electron relays. This is the maximum distance that allows for physiologically relevant electron-transfer rates (Moser et al. 2010; Page et al. 1999; Gray and Winkler 1996). Using this information, we visually identified residues in the vicinity of the iron-sulfur cluster that were conserved between *Cr*FDX1 and *Cf*FDX1 but not in *Cr*FDX2. We specifically focused on two amino acids located near the electron acceptor site of FDX1, namely F62 and Y95: (Fig. 2b shows the location of these residues).

In vitro hydrogen photo-production rate

To evaluate the effect of the selected mutated amino acid residues on CrFDX2 biochemical properties, we measured hydrogen photo-production rates driven by CrFDX1, CrFDX2, and the point-mutated versions of CrFDX2 (M62F, ∇95Y, and M62F/∇95Y) (see Table 2). In agreement with Peden et al. (2013), CrFDX1 promoted the highest hydrogen photo-production rate, 489 (±48) µmol H_2 µg Chl^{-1} h^{-1}, while CrFDX2 displayed a 5.6-fold lower rate (86 ± 11 µmol H_2 µg Chl^{-1} h^{-1}). Interestingly, each of the CrFDX2 point-mutants resulted in rates that were almost twofold higher than the native CrFDX2 (M62F, 150 ± 41; and ∇95Y, 134 ± 42 µmol H_2 µg Chl^{-1} h^{-1}), but lower than the CrFDX1 rates. This effect appears to be additive, as the CrFDX2 double mutant (M62F/∇95Y) displayed the highest rate among the three mutants (264 ± 69 µmol H_2 µg Chl^{-1} h^{-1}). The HYDA1 H_2 evolution rate with CrFDX2 M62F/∇95Y was threefold higher than with CrFDX2 WT, and half of that with CrFDX1. These data show that F62 and Y95 each function to support productive electron-transfer complexes between CrFDX1 and CrHYDA1 and, when engineered onto CrFDX2, confer it higher catalytic rates. In other words, mutations that introduce these CrFDX1 amino acid residues onto CrFDX2 are likely to induce similar structural changes in CrFDX2 to promote higher hydrogen production rates, closer to those measured with CrHYDA1.

In vitro NADPH photo-production kinetic parameters

The kinetic parameters K_m (µM), V_{max} (µmol NADPH µg Chl^{-1} h^{-1}) and k_{cat} (s^{-1}), of CrFDX1, CrFDX2, and the CrFDX2 point-mutants for the NADPH photo-production reaction were determined from the respective Lineweaver–Burk plots (see Table 3 and Supplemental Fig. 5). Interestingly, the V_{max} values for NADPH photo-production were similar for CrFDX1 and CrFDX2, at 185 (±68) and

177 (±47) µmol NADPH µg Chl^{-1} h^{-1}, respectively. However, the K_m for CrFDX2 (0.18 ± 0.01, µM) was significantly lower than that for CrFDX1 (0.40 ± 0.04, µM), indicating CrFDX2's higher affinity for CrFNR1. On the other hand, K_m values for each of the CrFDX2 mutants were higher than that for the native CrFDX2 (Table 3), with values of 0.69 ± 0.04 µM for the M62F mutant, 0.38 ± 0.03 µM for the ∇95Y mutant, and 3.44 ± 0.71 µM for the M62F/∇95Y double mutant. The calculated V_{max} values for the FNR-catalyzed NADPH production by the mutant proteins were 161 ± 26 µmol NADPH µg Chl^{-1} h^{-1} for the M62F mutant, 202 ± 10 µmol NADPH µg Chl^{-1} h^{-1} for the ∇95Y mutant, and 260 ± 33 µmol NADPH µg Chl^{-1} h^{-1} for the M62F/∇95Y double mutant. These values are very similar to those measured with either CrFDX1 or CrFDX2 WT proteins, considering the error bars. The catalytic efficiencies of CrFDX2 and CrFDX2 mutants in driving the CrFNR1-dependent reaction, k_{cat}/K_m, showed interesting trends compared to CrFDX1 (Table 3). Although CrFDX2 supported a slightly lower V_{max}, the lower K_m with CrFNR1 resulted in a twofold larger k_{cat}/K_m, indicating the formation of a more efficient catalytic complex. On the other hand, CrFDX2 M62F presented a fourfold lower k_{cat}/K_m compared to CrFDX2 and twofold lower than CrFDX1. The CrFDX2 ∇95Y variant led to a slightly higher V_{max} but lower k_{cat}/K_m, a value that is more similar to that measured with CrFDX1. When the M62F mutation was paired with ∇95Y in the CrFDX2 double mutant, the resulting variant supported the highest k_{cat}, but led to a large, 13-fold decrease in k_{cat}/K_m compared to CrFDX2. Overall, the kinetics suggest that CrFDX2, under growth conditions where it is present in equimolar amounts to CrFDX1, is better at electron transfer with FNR1 than CrFDX1, by virtue of forming a more efficient catalytic complex with FNR1. In contrast, CrFDX1 catalyzes higher rates of H_2 evolution, and the changes (although small) observed with the M62F and ∇95Y mutants of CrFDX2 are evidence for involvement of these residues in H_2 evolution.

Table 2 Hydrogen photo-production rates

Ferredoxin	Hydrogen Photo-production Rate (µmol H_2 µg Chl^{-1} h^{-1})
CrFDX1	489 ± 48
CrFDX2	86 ± 11
CrFDX2 (M62F)	150 ± 41
CrFDX2 (∇95Y)	134 ± 42
CrFDX2 (M62F/∇95Y)	264 ± 69

The CrFDX1, CrFDX2, and mutated CrFDX2 proteins used for the hydrogen photo-production assay were the cleaved forms purified from proteins over-expressed in *E. coli* from the respective FDX-TEVcs-GST-His constructs. Individual rates were calculated from four time points (approximately $t = 60, 180, 300$ and 420 min) and the averaged rates are shown

Table 3 Kinetic values for FDX-mediated NADPH photo-production in a reconstituted system

Ferredoxin	K_m NADP$^+$ (μM)	V_{max} NADP$^+$ (μmol NADPH μg Chl^{-1} h^{-1})	Turnover k_{cat} (s^{-1}) for NADP$^+$ reduction	Efficiency k_{cat}/K_m (M^{-1} s^{-1}) for NADP$^+$ reduction
*Cr*FDX1	0.40 ± 0.04	185 ± 68	668 ± 25	17×10^8
*Cr*FDX2	0.18 ± 0.01	177 ± 47	638 ± 17	35×10^8
*Cr*FDX2 (M62F)	0.69 ± 0.04	161 ± 26	581 ± 9	8.4×10^8
*Cr*FDX2 (∇95Y)	0.38 ± 0.03	202 ± 10	729 ± 37	19×10^8
*Cr*FDX2 (M62F/∇95Y)	3.44 ± 0.71	260 ± 33	939 ± 120	2.7×10^8

The FDX1, FDX2, and mutated FDX2 proteins used for the NADPH photo-production assay were prepared by TEV treatment of FDX-TEVcs-GST-His fusions. Both K_m and V_{max} values were calculated from three independent replicates using linear regression analyses of Lineweaver–Burk plots. Supplemental Fig. 5 shows the Lineweaver–Burk plots for the averaged rates. NADPH photo-production rates (V_{max}) are given in μmol NADPH μg Chl^{-1} h^{-1} with 1 mM FNR1 present and a 1-ml assay volume were calculated from the initial 15 min after mixing. The k_{cat} values were calculated at FDX concentrations of 1 mM

Midpoint redox potential determination

The midpoint redox potentials of the *Cr*FDX2 mutants were determined to test the effect of the mutations on the electron transfer properties of the [2Fe2S] cluster. Both of the single mutations shifted the potential more negative compared to *Cr*FDX2, with the M62F mutation giving the largest shift bringing it close to the midpoint potential of *Cr*FDX1 (Fig. 4, Table 4). Surprisingly, the double mutant did not show an additive shift of the single mutations but rather displayed a redox potential similar to that of the ∇95Y alone. While the overall rhombic signal assigned to the [2Fe2S] cluster was almost identical in all cases, slight shifts in the *g*-values were observed for the mutants. It should be noted that appearance of other small signals were observed; however, these are likely from the redox cocktail and formation of radical species during the course of reduction with NaDT. The shifts in the rhombic [2Fe2S]-cluster signal can be summarized by a subtle upfield energy shift from the *g*-values of *Cr*FDX2 ($g = 2.06$, 1.97, and 1.88) to the *g*-values of *Cr*FDX1 ($g = 2.05$, 1.96, and 1.88). Compared to ∇95Y ($g = 2.063$, 1.973, and 1.883) and M62F/∇95Y ($g = 2.060$, 1.969, and 1.883), M62 showed the largest shift ($g = 2.052$, 1.959, and 1.880) resulting in its overall signal to more closely align with *Cr*FDX1 (Fig. 4 inset). Interestingly, these trends match nicely to the midpoint potential shifts of the mutants and particularly for M62F may indicate an underlying role toward finely tuning the orientation and electronic properties of the cluster.

Discussion

Recently, we initiated efforts to fully characterize the Chlamydomonas FDX interaction network (Peden et al. 2013). We and others had shown previously that *Cr*FDX1 plays a predominant role as an electron carrier in the cell,

through electron-transfer and binding interactions with multiple partners (Noth et al. 2012; Peden et al. 2013; Terauchi et al. 2009; van Lis et al. 2013). Interestingly, *Cr*FDX2 was demonstrated to be capable of binding in vitro to some of the same electron partners and promoting similar redox reactions as *Cr*FDX1 (Noth et al. 2012; Peden et al. 2013; van Lis et al. 2013).

In order to determine and compare the characteristics and functions of the two *Cr*FDXs in more details, and to identify and study the nature of their interaction with other enzymes, we performed additional biochemical and biophysical assays on the two-purified proteins. The spectroscopy studies confirmed that both proteins are highly similar, showing typical [2Fe2S]-ferredoxin spectra (Supplemental Figs. 2, 3, and 4). We also grew crystals and solved the *Cr*FDX2 structure, which represents the first solved Chlamydomonas FDX structure. A structure of *Cr*FDX1 from *Chlorella fusca* was previously reported (Bes et al. 1999), and it was used for the visual identification of differences between *Cr*FDX1 and *Cr*FDX2. Five different amino acids located in the vicinity of the [2Fe2S] cluster and at the binding interface between both *Cr*FDXs and *Cr*HYDA1 were identified (Winkler et al. 2009a). As such, they have the potential to affect the binding properties of either of the two *Cr*FDXs, or possibly their electron transfer potentials to specific donors/acceptors. We mutated two residues in *Cr*FDX2 to resemble those present in *Cr*FDX1 and determined the effects on two reactions: NADP$^+$ reduction and H$_2$ photo-production.

The catalytic properties of each of our FDX mutants are different with respect to electron transport to *Cr*HYDA1 and *Cr*FNR1, as shown in Tables 2 and 3, respectively. We demonstrated that introduction of Y95 and mutation of *Cr*FDX2 M62 to phenylalanine directly affects its hydrogen and NADPH photo-production activity. The single *Cr*FDX2 M62F and ∇95Y mutants showed higher hydrogen photo-production rates than the *Cr*FDX2 WT protein, but not as high as that of *Cr*FDX1. This demonstrates that
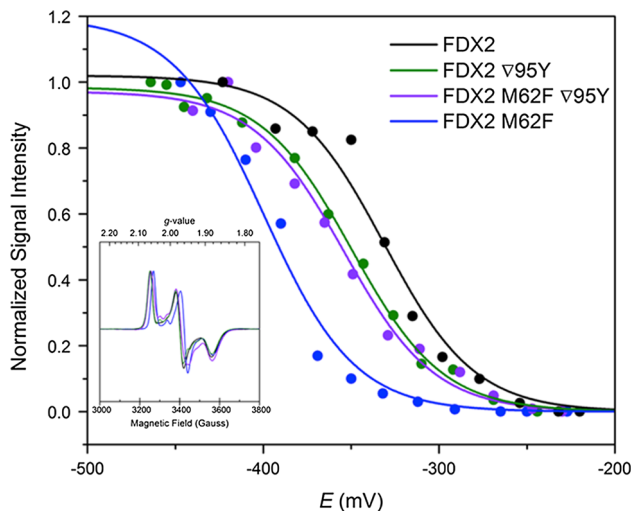
Fig. 4 Redox titrations of the [2Fe2S]-EPR signal (*inset*) from reduced *Cr*FDX2 wild type, ∇95Y, M62F/∇95Y, and M62F mutants. Each point reflects a measured EPR amplitude of the $g = 2.05/2.06$ peak for individual samples poised at particular potentials (E) vs NHE. The midpoint potentials were determined by fitting the potentiometric curves to the $n = 1$ electron form of the Nernst Equation

Table 4 The midpoint potentials of FDX2 mutants compared to *Cr*FDX1 and *Cr*FDX2 wild types

Ferredoxin	E_m (vs NHE)
*Cr*FDX1	−398[a]
*Cr*FDX2	−331[b] (−321[c])
*Cr*FDX2 (M62F)	−400
*Cr*FDX2 (∇95Y)	−350
*Cr*FDX2 (M62F/∇95Y)	−356

[a] Ref (Galván and Márquez 1985)

[b] This study

[c] Ref. (Terauchi et al. 2009)

both residues in *Cr*FDX1 promote high hydrogen production, either by affecting protein complex formation/stabilization, electron transfer, or both. This was to be expected from the structural results that showed the proximity of these residues to the *Cr*FDX: *Cr*HYDA1 binding interface (Fig. 2b). Interestingly, the double mutant was able to support hydrogen production at an even higher rate than either of the two single mutants and, in fact, twofold higher than the *Cr*FDX2 WT (Table 2). The additive effect of these mutations suggests that both residues in *Cr*FDX1 contribute to its high H_2 production. Indeed, both mutations resulted in shifts in the midpoint redox potentials of *Cr*FDX2 toward more negative values (Table 4), which favor electron transfer to *Cr*HYDA1.

We also tested the kinetics of WT and point-mutated *Cr*FDX2 proteins in NADPH photo-production. We show

that the presence of *Cr*FDX1 F62 and Y95 in *Cr*FDX2 affect NADPH production in opposite manners. The presence of F62 in *Cr*FDX2 interferes mostly with its binding affinity to *Cr*FNR (higher K_m compared to wild-type FDX2) and leads to a decrease in the turnover of NADPH production (k_{cat}). This could be due to the direct interaction between residue 62 and *Cr*FNR's FAD co-factor (Supplementary Fig. 4c, e), which may be weakened by the presence of methionine in this position. On the other hand, the deletion of Y95 from *Cr*FDX2 affects all kinetic parameters of the FNR-mediated reaction, as shown by an increase in its K_m, K_{cat} and catalytic efficiency (levels similar to those obtained with *Cr*FDX1) (Table 3). These residues are therefore important for the *Cr*FDX1: *Cr*FNR interaction and photo-reduction of NADP$^+$. It must be noted that others had shown that the *Cr*FNR has almost identical k_{cat}s in the presence of either *Cr*FDX1 or *Cr*FDX2, but the K_m for *Cr*FDX2 was almost sixfold lower than that for *Cr*FDX1, resulting in a sixfold higher catalytic efficiency for *Cr*FDX2 (Hurley et al. 1997; Vieira and Davis 1986). However, the reported values were derived from an assay that indirectly measured electron transfer between ferredoxin and *Cr*FNR using cytochrome c reductase activity; therefore their results are not directly comparable to ours.

The kinetics parameters observed for the *Cr*FDX2 double mutant seem to be a combined effect of the two single mutations, yielding a protein with a much higher K_m (as the single M62F mutant), but also high V_{max} (high rates of NADP reduction, as the single ∇95Y mutant) and high k_{cat} (higher catalytic efficiency, as the single ∇95Y mutant), although low catalytic efficiency. These differences are accompanied by structural differences at positions 62 and 95 in the *Cr*FDXs, which could partially account for the observed differences in kinetics. These observations are also consistent with the concept that subtle changes involving this particular structural region have significant effects in electron transfer within the functional catalytic complex. Indeed, all the mutations introduced at position 62 and 95 of *Cr*FDX2, singly or in combination led to changes in redox-midpoint potentials as compared to *Cr*FDX2. The EPR titration data (Table 4) showed that the E_m value of the ∇95Y *Cr*FDX2 mutant shifted more negatively, closer to the *Cr*FDX1 value (−350 vs −398 vs −331 mV for ∇95Y, *Cr*FDX1 and *Cr*FDX2, respectively). The double mutant M62F/∇95Y showed a similar pattern with an E_m of −350 mV where the single M62F mutant had midpoint potential of −400 mV almost identical to *Cr*FDX1 (−398 mV Terauchi et al. 2009).

In previous literature, certain amino acid residues were shown to be important specifically for the *Cr*FDX1/ *Cr*HYDA1 interaction, and to be critical for efficient electron transfer between these two proteins. *In silico* docking analysis and site-directed mutagenesis, for

instance, identified (among ten amino acid residues tested) CrHYDA1 K396, and FDX1 E122 (amino acid numbers represent the position in the protein prior to cleavage of the transit peptide) as the major contributors to the formation of the FDX-HYD1 complex (Winkler et al. 2010). Interestingly, the two CrHYDA1 and CrHYDA2 share conservation of the required lysine, and five CrFDXs (except for CrFDX3) contain the conserved glutamic acid residue. Residues D56 and F93 in FDX1 were also shown to be important for the CrFDX1-CrHYDA1 interaction; F93 together with E122 and Y126 was proposed to be involved in stabilizing the redox state of [2Fe2S] cluster of CrFDX1, suggesting their probable role in electron transfer between CrFDX1 and CrHYDA1 (Winkler et al. 2010). Indeed, when mutated to nonconserved residues, the respective recombinant proteins showed a decreased V_{max} for H_2 photo-production of more than threefold compared to the WT value (11).

Electrostatic interactions have also been demonstrated to be crucial for the interaction between ferredoxins and all their other target enzymes, such as FNR, FD:thioredoxins reductase, nitrite reductase, glutamate synthase, and sulfite reductase (Hanke and Mulo 2013). More specifically, CrFDX1 interaction-complex studies have provided evidence for the essential role of another conserved glutamate, E91, located in the short C-terminal tail of CrFDX1, and of a negatively charged patch, located in its most N-terminal α1-helix, which includes D25, E28, and E29. All four negatively charged residues are conserved only in CrFDX1, CrFDX2, and CrFDX5, out of the six CrFDXs (Terauchi et al. 2009). E91 is involved in forming complexes with nitrite reductase (NiR), glutamate synthetase (FDX-GOGAT), and the photosystem I subunit C (PSAC). Mutations of this residue in CrFDX1 diminish its catalytic activity in the reactions involving these enzymes (Fischer et al. 1998; GarciaSanchez et al. 1997). In addition, a triple D25A/E28Q/E29Q mutant protein showed less efficient interaction with those same three interacting enzymes (GarciaSanchez et al. 1997; Jacquot et al. 1997).

Besides electrostatic interactions, the midpoint redox potential of the two CrFDXs plays an important role in their physiological functions. Normally, CrFDX2 catalyzes nitrite reduction (Terauchi et al. 2009), a reaction with a midpoint redox potential of about −300 mV; $NADP^+$ reduction and H_2 production, on the other hand, are catalyzed by CrFDX1 in vivo, in reactions that require more negative redox potentials (−320 and −400 mV, respectively). It was shown that the presence of an aromatic residue at position 65 in Anabaena ferredoxin is essential for effective electron transfer with FNR (Hurley, cheng et al. 1993), and that natural variants of animal and bacterial FDXs in which methionine is replaced by phenylalanine show a shift in the E_m to more positive values

(Hurley et al. 1993a, b, 1997). We suspected that the switch from phenylalanine at residue 62 in CrFDX1 to methionine in CrFDX2 (Fig. 2b), in particular, was responsible for the significantly different CrFDX2 ability to catalyze NADPH and H_2 production. In this study, we measured and compared redox potential and kinetic parameters for the NADPH and H_2 photo-production between the CrFDX2 and the CrFDX2 M62F and ∇95Y mutants with those of CrFDX1. NADPH production, which involves $NADP^+ + 2H^+$ binding, involves a more complex reaction, since it requires the binding of both $NADP^+$ and $2H^+$ to the FDX/FNR complex when compared to the FDX/HYDA interaction which requires only the binding of $2H^+$. Finally, although our CrFDX2 crystal structure shows that both residues are located near the FDX [2Fe2S] cluster and could therefore influence the catalytic activity of FDX when in complex with FNR/HYDA, it seems that this is in fact organism dependent. In Anabaena, for example, FDX undergoes a conformational change at the level of the loop that contains F65 (the equivalent of F62 in Chlamydomonas) upon binding to FNR (Morales et al. 2000). Furthermore, this amino acid is proposed to be involved in the electronic coupling between the two redox centers (Hurley et al. 1993a). On the other hand, the maize leaf FDX/FNR crystal structure complex revealed that the equivalent amino acid of F65 (here Tyr 63) is neither in close contact with the [2Fe2S] cluster of the FDX, nor is between the two prosthetic groups from FNR (FAD) and FDX ([2Fe2S]) suggesting a different role in electron transfer to FNR for that residue (Kurisu et al. 2001). Unfortunately we do not have a crystal structure of the Chlamydomonas FDX/FNR complex to verify either mechanism. An alternative possible explanation for our kinetic data is that the mutations could interfere with PSI binding, which would further affect electron transfer to the FDXs. The data could therefore indicate that the mutations perturb the conformation of the CrPSI: CrFDX2 complex solely or in addition to the CrFDX2:CrHYDA1 complex. It is known that PSI subunits interact with CrFDX, although it remains unclear how many sites are present and/or available for FDX binding on CrPSI. Furthermore, no information regarding the K_m for CrPSI: Cr FDX electron transfer is available, although K_d values for WT and some PSI mutants ranging from 6 to 0.12 μM have been reported (Setif 2001; Setif et al. 2002). Finally, it must be noted that the error bars reflecting the double mutant data were particularly high, possibly due to the higher instability of the double mutant protein. The actual kinetic values must thus be taken only as representing a trend, not an actual number.

In summary, despite their high sequence similarity and comparable physical characteristics, CrFDX1 and CrFDX2 also exhibit structural differences that affect their electron-transfer function. A previous structural model predicted

differences in the surface charge distribution between the two proteins (Terauchi et al. 2009), and our CrFDX2 structure and biochemical results further show that the CrFDX2 M62 and CrFDX1 95Y residues make significant contributions to the binding interfaces of the respective CrFDXs with CrHYDA1 and CrFNR1, as well as affecting their redox potentials. These distinct differences must certainly contribute to the different in vivo specificities of the two proteins (Gou et al. 2006; Terauchi et al. 2009). In this report, we indirectly demonstrate that the CrFDX1 F62 and Y95 residues are important for hydrogen photo-production, as progressively increased hydrogen production rates are measured when these residues are introduced into CrFDX2. Residues F62 and Y95 also affect NADPH photo-production and have opposite impacts on the kinetic parameters of that reactions. We thus confirm that CrFDX2 can potentially replace CrFDX1 in CrFDX1-dependent reactions and that differences between the two proteins rely on differences between only a few amino acid residues.

References

Bertini I, Luchinat C, Provenzani A, Rosato A, Vasos PR (2002) Browsing gene banks for Fe2S2 ferredoxins and structural modeling of 88 plant-type sequences: an analysis of fold and function. Proteins 46:110–127

Bes MT, Parisini E, Inda LA, Saraiva LM, Peleato ML, Sheldrick GM (1999) Crystal structure determination at 1.4 A resolution of ferredoxin from the green alga *Chlorella fusca*. Structure 7:1201–1211 (**London, England : 1993**)

Chang CH, King PW, Ghirardi ML, Kim K (2007) Atomic resolution Modeling of the ferredoxin: FeFe hydrogenase complex from *Chlamydomonas reinhardtii*. Biophys J 93:3034–3045

Chen VB, Arendall WB 3rd, Headd JJ, Keedy DA, Immormino RM, Kapral GJ, Murray LW, Richardson JS, Richardson DC (2010a) MolProbity: all-atom structure validation for macromolecular crystallography. Acta Crystallogr D Biol Crystallogr 66:12–21

Chen VB, Arendall WB III, Headd JJ, Keedy DA, Immormino RM, Kapral GJ, Murray LW, Richardson JS, Richardson DC (2010b) MolProbity: all-atom structure validation for macromolecular crystallography. Acta Crystallogr Sect D Biol Crystallogr 66:12–21

Dutton PL (1978) Redox potentiometry: determination of midpoint potentials of oxidation-reduction components of biological electron-transfer systems. Methods Enzymol 54:411–435

Emsley P, Lohkamp B, Scott WG, Cowtan K (2010) Features and development of Coot. Acta Crystallogr D Biol Crystallogr 66:486–501

Engh RA, Huber R (1991) Accurate bond and angle parameters for X-Ray protein-structure refinement. Acta Crystallogr Sect A 47:392–400

Fischer N, Hippler M, Setif P, Jacquot JP, Rochaix JD (1998) The PsaC subunit of photosystem I provides an essential lysine residue for fast electron transfer to ferredoxin. EMBO J 17:849–858

Fish A, Danieli T, Ohad I, Nechushtai R, Livnah O (2005) Structural basis for the thermostability of ferredoxin from the cyanobacterium *Mastigocladus laminosus*. J Mol Biol 350:599–608

Fukuyama K (2004) Structure and function of plant-type ferredoxins. Photosynth Res 81:289–301

Galván F, Márquez A (1985) Physicochemical properties of ferredoxin from Chlamydomonas reinhardii. *Zeitschrift fur Naturforschung*. Sect C Biosci 40:373–378

GarciaSanchez MI, Gotor C, Jacquot JP, Stein M, Suzuki A, Vega JM (1997) Critical residues of *Chlamydomonas reinhardtii* ferredoxin for interaction with nitrite reductase and glutamate synthase revealed by site-directed mutagenesis. Eur J Biochem 250:364–368

Ghirardi ML, Zhang JP, Lee JW, Flynn T, Seibert M, Greenbaum E, Melis A (2000) Microalgae: a green source of renewable H_2. Trends Biotechnol 18:506–511

Gou P, Hanke GT, Kimata-Ariga Y, Standley DM, Kubo A, Taniguchi I, Nakamura H, Hase T (2006) Higher order structure contributes to specific differences in redox potential and electron transfer efficiency of root and leaf ferredoxins. Biochemistry 45:14389–14396

Gray HB, Winkler JR (1996) Electron transfer in proteins. Annual Review of Biochemistry 65:537–561

Hagen WR (2008) Biomolecular EPR spectroscopy. *CRC press* ISBN 978-1-4200-5957-1

Hanke G, Mulo P (2013) Plant type ferredoxins and ferredoxin-dependent metabolism. Plant Cell Environ 36:1071–1084

Harris EH (2009) The Chlamydomonas sourcebook, 2nd edn., Introduction to Chlamydomonas and its laboratory use, vol 2, Chap 7 Academic Press, Oxford, pp 217–255

Hase T, Wada K, Matsubara H (1976) Amino-acid sequence of major component of aphanothece-sacrum ferredoxin. J Biochem 79:329–343

Hurley JK, Cheng H, Xia B, Markley JL, Medina M, Gomezmoreno C, Tollin G (1993a) An aromatic amino-acid is required at position 65 in Anabaena ferredoxin for rapid electron transfer to ferredoxin NADP+ reductase. J Am Chem Soc 115:11698–11701

Hurley JK, Salamon Z, Meyer TE, Fitch JC, Cusanovich MA, Markley JL, Cheng H, Xia B, Chae YK, Medina M, Gomez-moreno C, Tollin G (1993b) Amino-acid residues in *Anabaena ferredoxin* crucial to interaction with ferredoxin NADP+ reductase site directed mutagenesis and laser flash photolysis. Biochemistry 32:9346–9354

Hurley JK, Weber-Main AM, Stankovich MT, Benning MM, Thoden JB, Vanhooke JL, Holden HM, Chae YK, Xia B, Cheng H, Markley JL, Martinez-Julvez M, Gomez-Moreno C, Schmeits JL, Tollin G (1997) Structure-function relationships in Anabaena ferredoxin: correlations between X-ray crystal structures, reduction potentials, and rate constants of electron transfer to ferredoxin:NADP+ reductase for site-specific ferredoxin mutants. Biochemistry 36:11100–11117

Hutson KG, Rogers LJ, Haslett BG, Boulter D, Cammack R (1978) Comparative studies on two ferredoxins from the cyanobacterium Nostoc strain MAC. Biochem J 172:465–477

Jacquot JP, Stein M, Suzuki A, Liottet S, Sandoz G, Miginiac-Maslow M (1997) Residue Glu-91 of *Chlamydomonas reinhardtii* ferredoxin is essential for electron transfer to ferredoxin-thioredoxin reductase. FEBS Lett 400:293–296

Kameda H, Hirabayashi K, Wada K, Fukuyama K (2011) Mapping of protein-protein interaction sites in the plant-type [2Fe-2S] ferredoxin. PLoS One 6:e21947

Kapust RB, Tozser J, Fox JD, Anderson DE, Cherry S, Copeland TD, Waugh DS (2001) Tobacco etch virus protease: mechanism of autolysis and rational design of stable mutants with wild-type catalytic proficiency. Protein Eng 14:993–1000

Krissinel E, Henrick K (2004) Secondary-structure matching (SSM), a new tool for fast protein structure alignment in three dimensions. Acta Crystallogr Sect D Biol Crystallogr 60:2256–2268

Kurisu G, Kusunoki M, Katoh E, Yamazaki T, Teshima K, Onda Y, Kimata-Ariga Y, Hase T (2001) Structure of the electron transfer complex between ferredoxin and ferredoxin-NADP(+) reductase. Nat Struct Biol 8:117–121

Matsubara H, Sasaki RM (1968) Spinach ferredoxin. II tryptic, chymotryptic, and thermolytic peptides, and complete amino acid sequence. J Biol Chem 243:1732–1757

Mayoral T, Martinez-Julvez M, Perez-Dorado I, Sanz-Aparicio J, Gomez-Moreno C, Medina M, Hermoso JA (2005) Structural analysis of interactions for complex formation between Ferredoxin-NADP+ reductase and its protein partners. Proteins 59:592–602

Meuser JE, D'Adamo S, Jinkerson RE, Mus F, Yang WQ, Ghirardi ML, Seibert M, Grossman AR, Posewitz MC (2012) Genetic disruption of both *Chlamydomonas reinhardtii* [FeFe]-hydrogenases: insight into the role of HYDA2 in H$_2$ production. Biochem Biophys Res Commun 417:704–709

Michoux F, Takasaka K, Boehm M, Nixon PJ, Murray JW (2010) Structure of CyanoP at 2.8 A: implications for the evolution and function of the PsbP subunit of photosystem II. Biochemistry 49:7411–7413

Morales R, Charon MH, Kachalova G, Serre L, Medina M, Gomez-Moreno C, Frey M (2000) A redox-dependent interaction between two electron-transfer partners involved in photosynthesis. Embo Reports 1:271–276

Moser CC, Anderson JLR, Dutton PL (2010) Guidelines for tunneling in enzymes. Bba Bioenerg 1797:1573–1586

Murshudov GN, Skubak P, Lebedev AA, Pannu NS, Steiner RA, Nicholls RA, Winn MD, Long F, Vagin AA (2011) REFMAC5 for the refinement of macromolecular crystal structures. Acta Crystallogr D Biol Crystallogr 67:355–367

Noth J, Krawietz D, Hemschemeier A, Happe T (2012) Pyruvate:ferredoxin oxidoreductase is coupled to light-independent hydrogen production in *Chlamydomonas reinhardtii*. J Biol Chem 288(6):4368–4377

Orme-Johnson WH (1973) Iron-sulfur proteins: structure and function. Annu Rev Biochem 42:159–204

Page CC, Moser CC, Chen XX, Dutton PL (1999) Natural engineering principles of electron tunnelling in biological oxidation-reduction. Nature 402:47–52

Pearson WR, Lipman DJ (1988) Improved tools for biological sequence comparison. Proc Natl Acad Sci USA 85:2444–2448

Peden EA, Boehm M, Mulder DW, Davis R, Old WM, King PW, Ghirardi ML, Dubini A (2013) Identification of global ferredoxin interaction networks in *Chlamydomonas reinhardtii*. J Biol Chem 288:35192–35209

Setif P (2001) Ferredoxin and flavodoxin reduction by photosystem I. Biochimica Et Biophysica Acta-Bioenerg 1507:161–179

Setif P, Fischer N, Lagoutte B, Bottin H, Rochaix JD (2002) The ferredoxin docking site of photosystem I. Biochim Et Biophys Acta-Bioenerg 1555:204–209

Stoll S, Schweiger A (2006) EasySpin, a comprehensive software package for spectral simulation and analysis in EPR. J Magn Reson 178:42–55

Terauchi AM, Lu SF, Zaffagnini M, Tappa S, Hirasawa M, Tripathy JN, Knaff DB, Farmer PJ, Lemaire SD, Hase T, Merchant SS (2009) Pattern of expression and substrate specificity of chloroplast ferredoxins from *Chlamydomonas reinhardtii*. J Biol Chem 284:25867–25878

Usselman RJ, Fielding AJ, Frerman FE, Watmough NJ, Eaton GR, Eaton SS (2008) Impact of mutations on the midpoint potential of the 4Fe-4S (+1,+2) cluster and on catalytic activity in electron transfer flavoprotein-ubiquinone oxidoreductase (ETF-QO). Biochemistry 47:92–100

Vagin A, Teplyakov A (2010) Molecular replacement with MOLREP. Acta Crystallogr D Biol Crystallogr 66:22–25

Van Lis R, Baffert C, Coute Y, Nitschke W, Atteia A (2013) *Chlamydomonas reinhardtii* chloroplasts contain a homodimeric pyruvate:ferredoxin oxidoreductase that functions with FDX1. Plant Physiol 161:57–71

Vieira BJ, Davis DJ (1986) Interaction of ferredoxin with ferredoxin:NADP reductase: effects of chemical modification of ferredoxin. Arch Biochem Biophys 247:140–146

Wada K, Kagamiyama H, Shin M, Matsubara H (1974) Ferredoxin from a blue-green alga, Aphanothece sacrum (Suringar) Okada. J Biochem 76:1217–1225

Winkler M, Kuhlgert S, Hippler M, Happe T (2009a) Characterization of the key step for light-driven hydrogen evolution in green algae. J Biol Chem 284:36620–36627

Winkler M, Kuhlgert S, Hippler M, Happe T (2009b) Characterization of the key step for light-driven hydrogen evolution in green algae. J Biol Chem 284:36620–36627

Winkler M, Hemschemeier A, Jacobs J, Stripp S, Happe T (2010) Multiple ferredoxin isoforms in *Chlamydomonas reinhardtii*—their role under stress conditions and biotechnological implications. Eur J Cell Biol 89:998–1004

Winn MD, Ballard CC, Cowtan KD, Dodson EJ, Emsley P, Evans PR, Keegan RM, Krissinel EB, Leslie AG, McCoy A, McNicholas SJ, Murshudov GN, Pannu NS, Potterton EA, Powell HR, Read RJ, Vagin A, Wilson KS (2011) Overview of the CCP4 suite and current developments. Acta Crystallogr Sect D Biol Crystallogr 67:235–242

Yacoby I, Tegler LT, Pochekailov S, Zhang S, King PW (2012) Optimized expression and purification for high-activity preparations of algal [FeFe]-hydrogenase. PLoS ONE 7:e35886